Additive Manufacturing 92 (2024) 104394

Contents lists available at ScienceDirect

Additive Manufacturing

journal homepage: www.elsevier.com/locate/addma

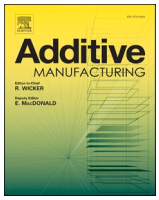

Design for disassembly: Using a multi-material approach in 3D printing for easier recycling strategies

Jakob Ecker [a], Robert Liska [b], Jürgen Stampfl [a,*]

[a] Institute of Materials Science and Technology, TU Wien, Getreidemarkt 9, Vienna 1060, Austria
[b] Institute of Applied Synthetic Chemistry, TU Wien, Getreidemarkt 9, Vienna 1060, Austria

ARTICLE INFO

Keywords:
Design for disassembly
Additive manufacturing
Recycling
DLP
Stereolithography

ABSTRACT

Due to the rapid expansion of the electronics sector, e-waste is becoming a growing issue that requires immediate attention. In particular, the complex assemblies and miniaturisation of these devices makes it difficult to recycle them properly. Additive manufacturing (AM), also known as 3D printing, offers a potential solution to this problem. The ability to print structures in µm- range makes it possible to print and manufacture electronic components in such a way that predetermined breaking points can be incorporated. Parts printed in this way are subject to the concept of *Design for Disassembly*, which describes the production of multi-material compounds or composites that can be easily separated or recycled. Using a multi-material approach in combination with Thermally Expandable Microspheres (TEMs) and processed by 3D printing, we produced easily separable compounds on demand. The compounds were characterized regarding their (thermo)mechanical behaviour. The study investigated the influence of the printed separation layer on the mechanical properties of the overall compound for various layer orientations. The printed parts were separated using heat as an external impulse, without requiring extensive force. This was achieved by subjecting the parts to a temperature of 200 °C for 10 minutes in a conventional oven.

1. Introduction

The recent technological advancements have enabled the production of electrical devices, including consumer electronics and batteries, with improved performance and increased output. These products are used in our everyday lives, and due to the growing population, they are being produced more frequently and rapidly. However, the increasing number of electrical devices is inevitably leading to a rise in electronic waste in the near future. The United Nations University has published a report on the generation of e-waste from 2019 with a forecast for 2030 [1]. In 2022, an estimated 59.4 million tonnes of e-waste were generated, with only approximately 17 % being reported as properly collected and recycled. It shows that the amount increases each year to a new maximum. One reason for these low recycling rates is the complexity and architecture of today's electronic devices [2]. All devices are composed of multi-material components. To ensure proper recycling, it is necessary to collect and sort all materials as effectively as possible. However, for optimum performance, all materials must be tightly assembled within the device. This can make it difficult to remove the inner materials once the equipment is no longer in use. Therefore, dismantling is an important step in the overall process to achieve proper recyclability rates. Common methods, especially in developing countries, still involve the use of manual tools (such as screwdrivers, pliers, or hammers), where the smaller the parts, the more difficult they can be to dismantle. This is very time and energy consuming, and many items end up in landfills [3,4]. Without proper recycling strategies, valuable resources in electronic components, such as noble metals or rare earth elements, can be lost.

As a first approach to achieving higher rates, the concept of "Design for Disassembly" (DfD) is demonstrated in this paper. DfD highlights the potential for products, or multi-material components to be easily separated and recycled. Using a multi-material approach, a thin layer of a "Disassembly material" (referred to as DfD material) is incorporated into a component. While the DfD material is not intended to affect the (thermo)mechanical properties of the component, it can be triggered by an external impulse, resulting in the activation of the DfD material and the disassembly of the component. This procedure facilitates disassembly and ensures that all internal parts can be easily removed when it comes to the end of life of the device.

Additive manufacturing, commonly known as 3D printing, offers

* Corresponding author.
E-mail address: juergen.stampfl@tuwien.ac.at (J. Stampfl).

https://doi.org/10.1016/j.addma.2024.104394
Received 5 March 2024; Received in revised form 26 August 2024; Accepted 26 August 2024
Available online 28 August 2024

several advantages to apply DfD to electronic components. In this study, vat photopolymerization is employed as a 3D printing method, whereby a liquid resin is cured in a layer-by-layer manner. This can be done either with a laser (stereolithography) or with a Digital Light Projection (DLP) engine [5]. In particular, the ability to produce features in the micrometre range, the freedom of geometric design, and the ability to process a range of thermoset polymers are the crucial advantages of the vat photopolymerization technique, which help to realize DfD concepts [5,6].

In the context of DfD, AM assembles different materials in a very small space to produce multi- material compounds. Several research groups are currently investigating the field of multi- material printing, and machines are already commercially available [7–9]. Although AM enables the straightforward processing of disassemblable components, the technology necessitates the development of innovative material concepts and compounds to fully realise its potential. The chemical nature of the DfD material is highly dependent on the external impulse used to initiate the disassembly [10]. A thermal impulse is particularly desirable in this case due to its ease of implementation in industry. The DfD concept has already been successfully implemented, by a chemical approach, for polymers by incorporating thermolabile crosslinkers into the polymer network, as demonstrated by several research groups [11–14]. A different physical approach is the use of Thermally Expandable Microspheres (TEMs) as disassembly agent. Here, tiny thermoplastic capsules (~ 5–20 μm in diameter), which contain a certain amount of a gaseous hydrocarbon, can expand up to 60x its original volume, when heated up. The thermoplastic shell gets softer and makes it possible for the gas to expand completely [15]. These particles are widely used in several industries like in polymer processing, inks and pigments, or food packaging [16]. However, they have already found their way into research and the automotive industry to be used as a dismantling agent between adhesive joints and for dismantling vehicles at the end of their life [17,18]. When using this approach for 3D printed polymer parts, it is necessary to adjust both materials to each other. The DfD material must reach its glass transition temperature (T_g) before the TEMs are activated but must lose enough energy to be easily separated by the TEMs. Yet, the DfD material must not affect the (thermo)mechanical properties of the part as a whole when in use but should only be activated by the external stimulus. This ensures that the component can be used until the end of its duration but can also be recycled afterwards.

The aim of this paper is to present the concept of Design for Disassembly and its realisation through 3D printing. Therefore, multi-material compounds (made of a DfD material and a matrix material A) were printed and tested for their (thermo)mechanical behaviour and disassembly ability. In particular it should raise awareness of the use of modern technologies with the aim of realising easier recycling strategies for electrical equipment.

2. Design for disassembly applied for electronic waste (e-waste)

2.1. Design for assembly / disassembly

The aim of this paper is to introduce the concept of DfD for 3D printed components in the electronics sector. Nevertheless, the concept itself is not a novel one and is undergoing a process of evolution and improvement [19,20]. In the early 1990s, Boothroyd et al. published a comprehensive review of the evolution of Design for Assembly (DfA) and Design for Disassembly (DfD) practices. The review provided a detailed summary of the origins of these practices, tracing them back to the 1960s. However, this was just the point at which companies began to develop guidelines for their product design [19]. It has been observed that integrating the DfA and DfD concepts within a single component can be challenging and contrary. This has led to the perception that DfA strategies may pose difficulties in later disassembly [20]. To give an example, fastening with rivets are conducive to the DfA concept but not to DfD, whereas the deployment of screws is the antithesis for this. Both concepts can be advantageous for stacking, however, adhesives are not considered suitable for DfA and DfD. The objective has consistently been to integrate the two concepts into a single component. This integration is intended to facilitate easy assembly, reduce waste, increase recycling, and reduce resource demand. To facilitate the disassembly of plastic components, the GE plastics has also published a set of guidelines outlining the procedures for applying these concepts to plastic compounds [19]. A number of considerations were highlighted, including the minimisation of assembly operations, the reduction of waste production, and the avoidance of secondary finishing operations, to name a few of them.

Over time, research groups and companies have been engaged in the process of optimising those concepts for certain products and processes. The research presented here encompasses case studies of specific consumer electronics products, namely Shu-Kai S. Fan et al. have conducted a cost analysis of notebooks and W.D. Li et al. have studied liquid crystal displays. Favi et al. have developed software for the quantitative assessment of the disassemblability and recyclability of mechatronic products, while Palmieri et al. have taken a look into the automatization of the process for the end-of-life management of electronic boards [21–25].

Although the assembly of additive manufactured parts has consistently been a significant concern, contributing to the strengths of this technique, this work will now focus on the disassembly aspect [26,27].

2.2. State of the art recycling of e-waste

With an annual growth rate of 3–5 %, electronic waste represents one of the fastest-growing solid waste streams currently [28]. In 2019, the production of e-waste was particularly increased by the categories of small electronic devices, including headphones, music toys, alarms, speakers, and similar items, as well as small IT and telecommunication devices. The aforementioned entities collectively accounted for approximately 22.1 million metric tons of e-waste [29]. Liu et al. outlined the general composition of e-waste, which is estimated to comprise approximately 47 wt% iron and steel, 21 wt% plastics, 7 wt% copper, and 5 wt% glass[28]. Additionally, other materials such as wood, plywood, concrete, and ceramics may also be present. However, the remainder of the waste can contain precious metals (e.g., gold, silver platinum, palladium) and rare earth elements, which are a significant factor in the recycling motivation [28]. Furthermore, it was highlighted that the recycling costs of metals from this waste is even below the costs of mining the crude ore, which renders recycling even more attractive for exploitation. The total value of recyclable materials derived from e-waste is estimated to be approximately 57 billion USD [1].

The current State of the Art strategy for the recycling of e-waste is comprised of several stages. Starting with the collection and transportation of the waste, the subsequent phase is that of safe disassembly. Once the disassembly process is complete, the sorting and enrichment phase is initiated, which is followed by the material regeneration phase [28,30].

The disassembly process remains a manual operation, necessitating the use of tools, due to the variety in structure of the electronic components [4,28]. The dismantling stage is a crucial step of the overall process, as it ensures the removal of toxic and harmful components prior to sorting and crushing. Additionally, it enables the recovery of components from electrical devices, which can be repurposed for alternative applications. Once the disassembly process is complete, the remaining components are crushed and separated using a variety of techniques, including magnetic force, gravity, eddy currents, and airflow. The separated materials can then be manufactured into new functional materials or products or used for energy recovery. In considering the recycling process, it is essential to take into account the pollutant treatment requirements at each stage. Besides hazardous and toxic compounds, which can occur in the waste, the utilisation of techniques such as shredding, mechanical cutting and crushing during the

dismantling process has been demonstrated to result in the emission of fine and ultrafine particles [31].

2.3. Role of design for disassembly (DfD) in the recycling process

The recycling of e-waste includes various and complex steps, each of which can and should be optimised and improved to yield the greatest possible resource recovery. As a contribution to this process, the introduced Design for Disassembly concept (DfD) should be applied to the dismantling stage, enhancing the procedure. This concept can contribute to the optimisation of this stage via two factors;

As previously outlined in the introduction and chapter 2.1, the dismantling of the components necessitates the utilisation of manual tools due to their complex design and structure. In this regard, the deployment of DfD can facilitate, automatise, and accelerate the dismantling process and contributes to the minimisation of the quantity of waste that requires complete shredding.

The second contribution of DfD is related to the treatment of pollutants during the shredding process. Lopez at al. demonstrated that these techniques can result in the release of fine and ultrafine particles [31]. The pre-step in separation reduces the amount of waste that needs to be shredded, which can subsequently lead to a reduction in the occurrence of those emissions.

2.4. DfD layer

The DfD layer plays an essential role in the proposed concept, with the objective of facilitating the separation of all mentioned components and specimens upon heating. It serves as the vulnerable point within a component, which can be triggered when necessary. Its capacity to undergo a pronounced transformation in thermomechanical properties upon heating provides the TEMs within the system with the opportunity to fully expand with ease, thereby makes the separation possible (Fig. 1). To avoid any adverse effects that the DfD material may exert on the whole component, it is essential to select a layer with a thickness as thin as possible. The layer thickness was selected to be 4×50 µm, resulting in an ultimate layer thickness of 200 µm. This thickness was deemed to provide an optimal balance between sufficient adhesion between the materials, the thickness of the DfD material, and sufficient space for the TEMs in each layer, while the layers remained inactivated.

3. Materials and methods

3.1. Materials and formulation preparation

The matrix material (Type A) was prepared from a high molecular weight urethane polyester di-methacrylate (Bomar XR-741-SM, purchased by Dymax, USA) and hydroxyethyl methacrylate (HEMA, purchased by Sigma Aldrich, Vienna, Austria). Diphenyl(2,4,6-trimethylbenzol) phosphinoxid (TPO) was used as radical photoinitiator and was kindly provided by Archem as a gift. Quinoline Yellow SS acted as absorber and was purchased from Sigma Aldrich Vienna, Austria. The inhibitor (Pyrogallol) was purchased by Sigma-Aldrich (Vienna, Austria). Thermally Expandable Microspheres (TEMs) (Expancel® 909 DU 80) were gladly provided by Nouryon, Amsterdam, Netherlands. The TEMs have a particle size of approximately 18–24 µm in their pristine state and around 80 µm in their expanded form. The temperature range at which the TEMs begin to expand is 118–128 °C (T_{start}), while the temperature range at which they begin to lose their functionality is 178–187 °C (T_{max}). The high T_{start} temperature was selected to avoid spontaneous expansion due to polymerization heat or post-curing.

The photopolymerizable formulation from which Type A was prepared consisted of 65 wt% Bomar and 35 wt% HEMA. In respect to that formulation, 0.1 wt% of TPO and 0.025 wt% of Quinoline Yellow SS was added. Every component of the formulation was put together, preheated in an oven at 60 °C, and mixed in a Speed Mixer™ (DAC 150FVZ, Hauschild and Co. KG, Hamm, Germany) for 10 min at a speed of 3500 rotations per minute. As last step the formulation was degassed in a vacuum chamber.

The DfD material was a mixture of 1,3,5-triallyl-1,3,5-triazin-2,4,6 (1H,3H,5H)trion (**TTT**, Sigma Aldrich, Vienna, Austria) and the trifunctional thiol tris [2-(3-mercaptopropionyloxy ethyl) isocyanurate (**TEMPIC**, purchased by Bruno Bock, Germany). TPO was again utilized as the photoinitiator. The DfD formulation consisted of 1 part TEMPIC and 1.3 parts TTT. 1 wt% of TPO and 0.01 wt% Pyrogallol were added additionally.

The photoinitiator and inhibitor were dissolved in TTT before the addition of the thiol TEMPIC. After vortexing the formulation, it was put into a supersonic bath for 15 min.

To prepare the formulations containing TEMs, the DfD formulation was slightly heated to reduce the viscosity before the TEMs were added. The sufficient distribution of the particles was achieved by vortexing the formulation for 10 min and then subjecting it to an ultra-sonic bath for 15 min. The DfD formulation contained either 2, 5, or 10 wt% of TEMs. In the study conducted by Banea et al., concentrations between 5 wt% and 25 wt% were chosen for epoxy adhesives [32]. However, due to the considerable impact on viscosity and exposure tests, concentrations well below 25 wt% were selected and tested.

3.2. 3D printer

The printing was performed using a self-developed 3D DLP printer at TU Wien, consisting of a rotational, tiltable, and heatable vat, a coating blade, and a movable bottom up printhead (Fig. 2).

The combination of a heatable vat and a coating blade enabled the printing of resin with high viscosities that would otherwise not be possible to process at room temperature. The tiltable vat reduced the peel forces after the removal of each layer from the vat resulting in less stress for the printed part. As light source and imaging tool a light engine (Luxbeam 4600, Visitech Engineering GmbH, Wetzlar, Germany) with a wavelength of $\lambda = 375$ nm was used. The engine reached a light intensity of 25 mW cm $^{-2}$ at the surface of the printing vat. The system could provide a theoretical resolution of 10 µm in vertical (z) axes. Yet due to the diameter of the TEMs (~ 20 µm), 50 µm was chosen as a satisfying compromise between speed, resolution, and accuracy. For the plane axes, a resolution of 50 µm was possible. While material A could be printed at room temperature, the temperature of the vat for the DfD material was raised to 60 °C to reduce its viscosity. As the glass transition temperature of material A was well above 60 °C, as was the T_{start} of the TEMs, the temperature increase for the DfD material did not generally affect the component.

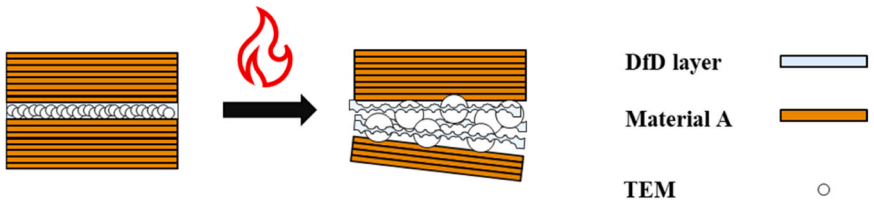

Fig. 1. Role of the DfD material within a component.

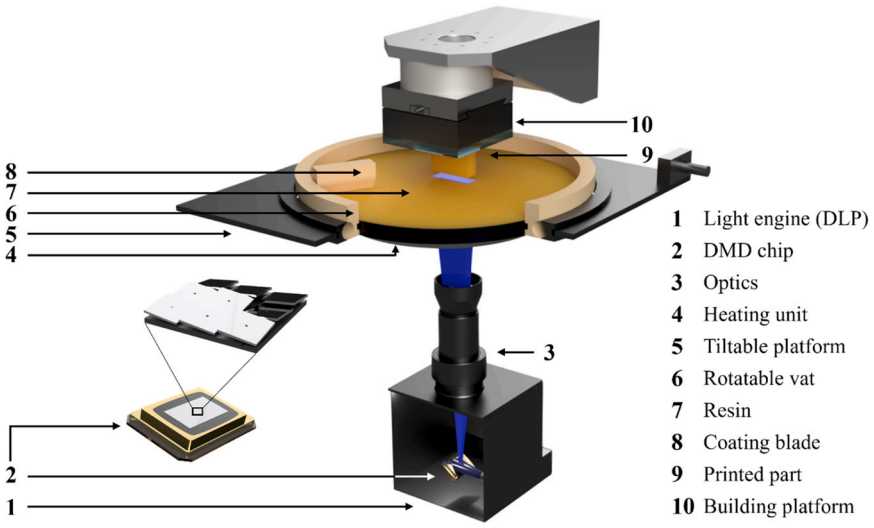

Fig. 2. Schematic setup of the used 3D printing system developed by TU Wien.

3.3. Sample preparation and orientation

To perform different (thermo)mechanical tests, suitable test geometries were printed according to ISO / ASTM 52921 in YXZ, YZX, and ZXY orientation (Fig. 3). Depending on the orientation, the DfD material was always placed in the middle of the specimen. All specimens were printed with a layer height of 50 µm.

Initially, one half of the specimen, comprising of Type A, was printed. Subsequently, four layers of the DfD material were incorporated, resulting in a total layer thickness of 200 µm of DfD material for each sample. The remaining half was again printed with Type A. An overall number of five test groups was prepared where the groups differed in their material combination and their amount of TEMs added to the DfD layer. Printing every group in three different layer directions resulted in an overall number of 15 sample sets.

As characterization, tensile test, DMA, and dynstat impact strength were chosen, to determine the (thermo)mechanical properties. To ensure complete conversion all specimens were post-cured for 300 s in an Uvitron International INTELLI-RAY 600 UV-oven with a 320 – 500 nm Hg broadband UV lamp (600 W; UV-A: 125 mW cm^{-2}; Vis: 125 mW cm^{-2}). During the post-curing phase, the temperature of the oven increased from 44 °C (idle mode) to 65 °C within 300 seconds as a consequence of the heat generated by the UV lamp. The precise temperature increase can be seen in the SI.

The printed parts and specimens were designed using CAD software (Autodesk Fusion 360, California, USA).

All formulations and specimens were mixed and prepared in a yellow-light laboratory.

3.4. Viscosity measurements

Viscosity measurements were performed on the formulations of material A, the DfD material, and all formulations containing TEMs using an Anton Paar MCR 300 equipped with a Peltier temperature control unit and a PP-25–1 measuring unit. The sample, which was approximately 80 – 150 µL, was placed on the element with a 48 µm gap between the bottom and the stamp. The shear rate was increased from 0 to 100 s^{-1} within 50 s and then kept steady at this value. Measurement points were taken every 5 s during the increase, resulting in 10 data points. Measurements were taken at a rate of 100 s^{-1}, with a measurement point recorded every 10 s leading to a total of 5 data points. The samples were measured both at room temperature and 60 °C, which was the final temperature at which the DfD material was printed. Each measurement was performed three times.

3.5. Scanning electron microscopy (SEM)

SEM images were captured using a Zeiss EVO 10 with a SmartSEM software and an Everhart-Thornley secondary electron detector. The acceleration voltage was set to 5 kV. To ensure proper conductivity, all samples were sputtered with a fine layer of gold and placed on a conductive carbon pad.

3.6. Digital light microscope

Digital light microscope images were taken with a 2.4-inch HDMI Digital Microscope with 1080 P HDMI output and a magnification range of 10x to 220x.

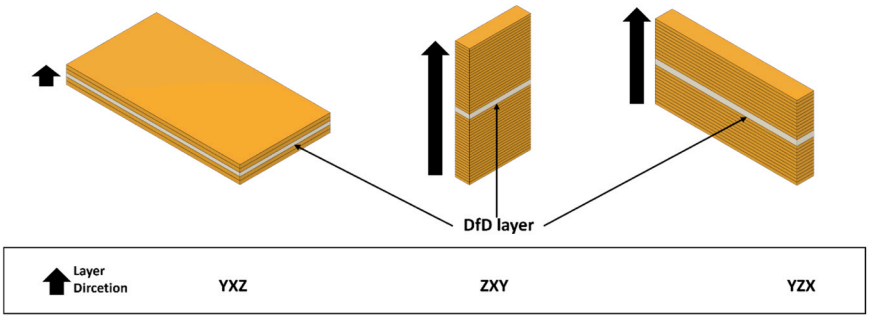

Fig. 3. Orientations and layer directions of the printed specimens (from the left to the right; YXZ, ZXY, and YZX orientation) with the additional DfD material in between.

3.7. Tensile test

Tensile tests were performed on a Zwick Z050 (Zwick Roell, Ulm, Germany) with a test speed of 5 mm min^{-1} and a 2.5 kN load cell. The test was executed according to ISO 527–1:2012, with specimens of B5 geometry, wherein the DfD layer was maintained at a consistent thickness of 200 µm. All tests were performed with sets of eight specimen.

3.8. DMA (Dynamic mechanical analysis)

DMA specimens were analysed using a DMA Q800 (TA Instruments, New Castle, USA) in a temperature range of −50–150 °C and a heating rate of 3 °C per min. The frequency was set to 1 Hz with an amplitude of 10 µm. The preload force was set to 0.1 N. For all specimens, the max of the tanδ peak was used to determine the glass transition temperature (T_g). For specimens containing the DfD material, the maximum of the loss modulus curve was also taken into account. The measurement was conducted in the multi-frequency-strain module and 3-point bending mode.

3.9. Dynstat impact strength

The Dynstat test was performed according to DIN 53435 on a Karl Frank GmbH Dynstat device, Type 573 using a 10 kpcm hammer with a pendulum impact tester. This kind of test is useful for unnotched specimens with sample geometries that are smaller than those required for more commonly used Charpy- or Izod-tests. For Dynstat, the specimens are held on one side over the entire width between two abutments [33]. All specimen types were subjected to testing using eight samples.

3.10. Disassembly experiments

The specimens were disassembled in a Binder drying oven (Tuttlingen, Germany) by placing them at 200 °C for 10 minutes and allowing them to cool to room temperature. The temperature was set slightly above the T_{max} temperature of the TEMs (178–187 °C) to ensure complete expansion. The 10-minute heating period was deemed sufficient to achieve a complete up-heating of the polymer to the desired temperature. For the demonstration video of the Molex cable connector, the connector was placed in a high-temperature oven equipped with a visible window glass (HTM Reetz GmbH, Berlin, Germany).

4. Results

4.1. Material selection and specimens

Subsequent results were obtained with the selected and reported materials and specimens. Material A was chosen as the hard matrix material of the specimens, to mimic the shell of an electronic device (Fig. 4).

The Disassembly material (DfD material) was used to create a weak spot within the matrix material. This allowed the specimens to be dismantled at higher temperatures with ease. Specimen Type A was solely made from material A. Specimen Type AB consisted of a fine DfD layer between two blocks of material A. Type AB-2 wt, −5 wt, and −10 wt had the same assembly than AB, but with the addition of the specified amount of TEMs in the DfD layer. For the upcoming rheological and (thermo)mechanical tests, the following formulations and specimens were prepared;

- Liquid formulations of material A, the DfD material, and the DfD material containing the specified amount of TEMs
- Eight tensile specimens (ISO 527 type B5)
- Eight specimens (cuboid shaped, 10 ×3 x 15 mm^3) for Dynstat impact strength
- One specimen (cube shaped, 5 ×2 x 26 mm^3) for dynamic mechanical analysis (DMA)
- One Molex cable connector as demonstration object

The incorporation of the DfD layer did not change the overall thickness of the specimens. This was due to the substitution of the middle layers of Type A with the DfD material, rather than an addition.

Two sets of the same orientation and group were always printed, tested, and compared to each other. The first set was tested directly at room temperature. The second set was heated to 200 °C, held for 10 minutes and then cooled before being tested at RT. This procedure was carried out to activate the TEMs and investigate the effect of heat treatment on the DfD material. The DMA specimens were not heated before to measurement.

All printed parts and specimens were designed with a CAD software

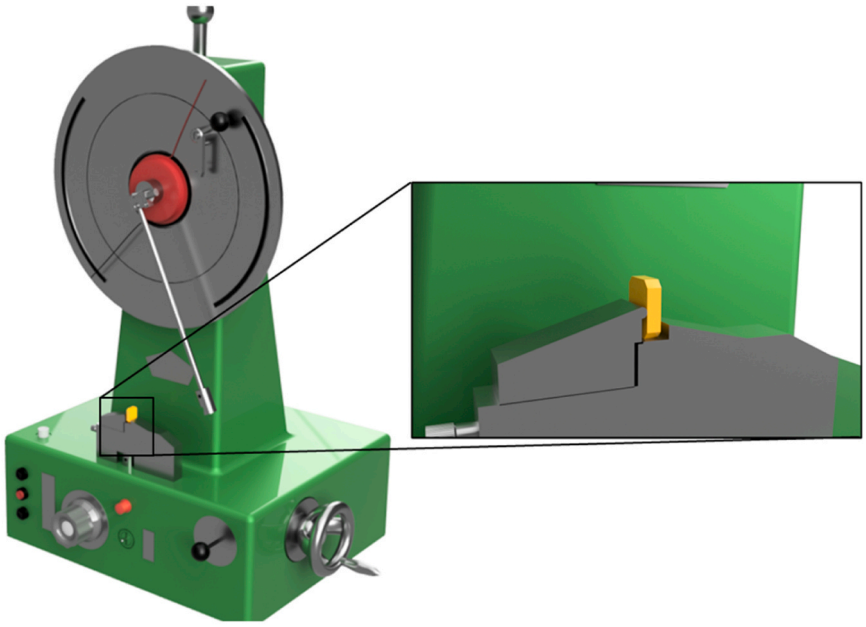

Fig. 4. The arrangement of the Dynstat test comprises two abutments (grey) that hold the specimen (yellow) over the entire width.

(Autodesk Fusion 360, California, USA).

4.2. Viscosity measurements

Viscosity is a crucial parameter for the processability of formulations in light-based additive manufacturing techniques. For commercial printers, resins should not exceed a viscosity of 2 Pa s for printability [34]. However, the printer used in this case can process formulations up to 20 Pa s due to its coating blade and heatable vat.

Both, the DfD formulation and material A had viscosities that could be processed at room temperature (Fig. 5). The DfD formulation had a viscosity of approximately 13 Pa s, while material A had a viscosity of ~ 0.6 Pa s.

However, all samples containing TEMs exhibited significantly higher viscosities, with the 10 wt formulation reaching up to almost 25 Pa s at room temperature. Every formulation with TEMs exceeded the threshold viscosity of 20 Pa s. Although it is possible to process formulations with a viscosity of 20 Pa s with the system used, lower viscosities are still desirable for the workflow and the quality of the printed parts. The addition of 2 wt% TEMs increased the viscosity from 13 Pa s to ~ 20 Pa s. Higher amounts of TEMs resulted in further increases in viscosity. At higher temperatures, all formulations exhibited a different trend. They showed significantly lower viscosities when heated up to 60 °C, falling within the range of material A (0.4 Pa s – 1 Pa s). An increase of 35 °C was sufficient to reduce their viscosities to 6 % of the original 25 °C value. At 60 °C, every formulation was easily processed without any issues.

4.3. Tensile test

4.3.1. YXZ orientation

The YXZ orientation group exhibited the largest surface layer of all orientations. This resulted in the highest amount of DfD material within the YXZ specimens (Fig. 6**a**). Although the DfD material had only a minimal effect on the tensile strength in comparison to Specimen Type A, the addition of TEMs led to a slight reduction.

Nevertheless, the specimens retained approximately 84 % of their initial strength even with 10 wt% of the TEMs in the DfD material (Fig. 6**b**). Increasing the quantity of TEMs did not lead to a significant reduction in tensile strength anymore. Initially, it appeared that Specimen Type AB had a superior elongation at break. However, given the high standard deviation of AB, no definitive conclusion could be drawn. Generally speaking, all groups exhibited comparable elongation at breaks when tested under room temperature conditions.

The heat-treated specimens displayed a comparable pattern with corresponding values for the tensile strength of A, AB, and AB-2 wt (Fig. 6**c**). Notably, the process caused reduction in the elongation at break for all heated-up samples due to the embrittlement of the specimens due to the intrinsic heat treatment.

The graph plots for AB-5 wt and AB-10 wt were not available as the samples experienced complete separation during the 10-minute exposure to 200 °C in the oven. As a result, tensile testing could not be performed on the specimens.

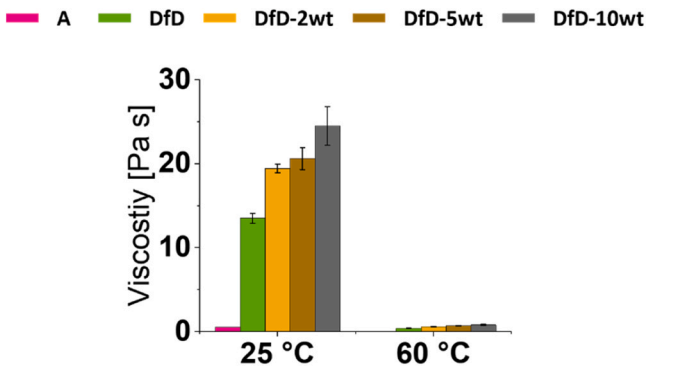

Fig. 6. Viscosity measurements of all formulations with and without TEMs at 25 °C and 60 °C. The shear rate was kept constant at 100 s^{-1}.

4.3.2. YZX orientation

In the YZX orientation, the DfD layers were placed along the entire specimen in a rectangular geometry. (Fig. 7**a**). This group demonstrated the lowest effect of the DfD material and TEMs on Specimen Type A. While the tensile strengths were comparable across all test groups, the elongation at breaks varied between 4 % and 12 % (Fig. 7**b**).

All heat-treated samples exposed markedly weaker tensile strengths (down to ~ 66 % of the initial strength) and elongations (~ 42 % of the initial elongation at break) than their untreated counterparts (Fig. 7**c**). The reduction can be traced back to the peeling forces during the printing process, which resulted in a minor change of symmetry within the samples. Due to the more brittle characteristics obtained by the heat treatment, their unsymmetrical contours make it more prone to failure. Despite these limitations, the samples comprising of 5 wt% and 10 wt% TEMs were effectively separated.

4.3.3. ZXY orientation

In the ZXY orientation, the specimens were printed upright. This resulted in the smallest area for the DfD material, also with a rectangular geometry (Fig. 8**a**).

The ZXY oriented samples displayed the most significant change when compared to Specimen Type A. Although the effect of the supplementary materials in the YXZ and YZX orientation was minimal, the specimens here experienced a substantial reduction in both tensile strength and elongation at break (Fig. 8**b, c**). The inclusion of the DfD material and TEMs caused a drop down to ~ 23 % of the original strength and ~ 29 % of the original elongation at break. This outcome was predictable since the tensile test's applied force is perpendicular to the layer direction. The surfaces are solely linked to one another through

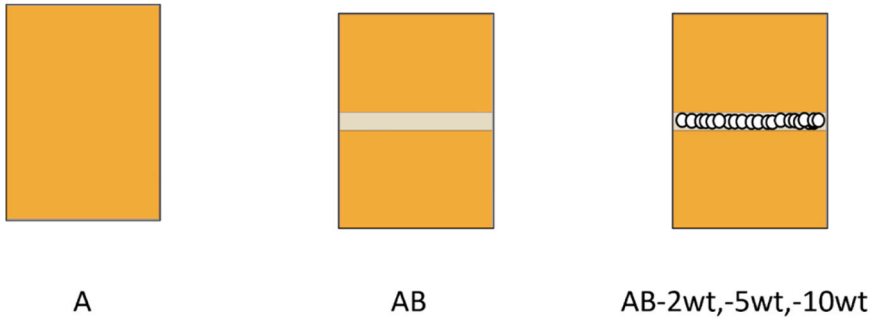

Fig. 5. Schematic samples in ZXY orientation representing the different test groups. Type A was made solely from material A, whereas AB contained the DfD material in between. Samples AB-2 wt, −5 wt, and −10 wt contained the DfD material as well the specified amount of TEMs within the DfD material.

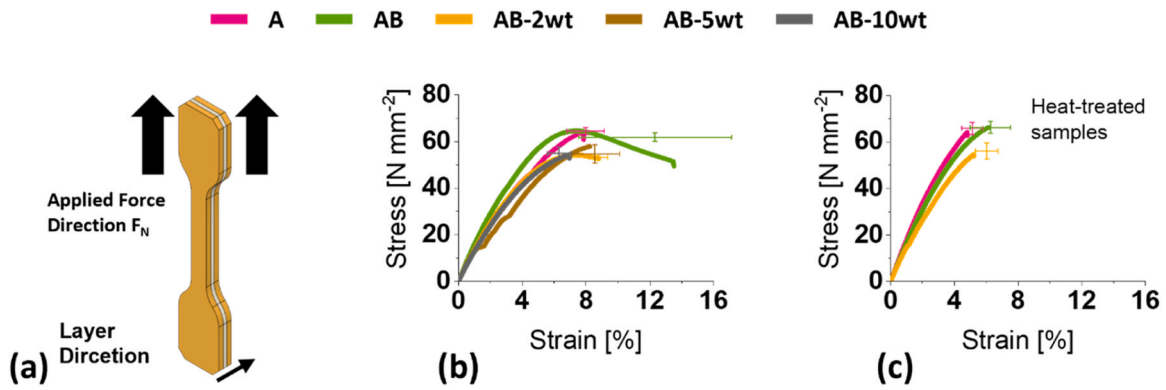

Fig. 7. Printing and applied force orientation of the YXZ specimens (a), results of the tensile tests at room temperature (b), and of the heat-treated samples (c).

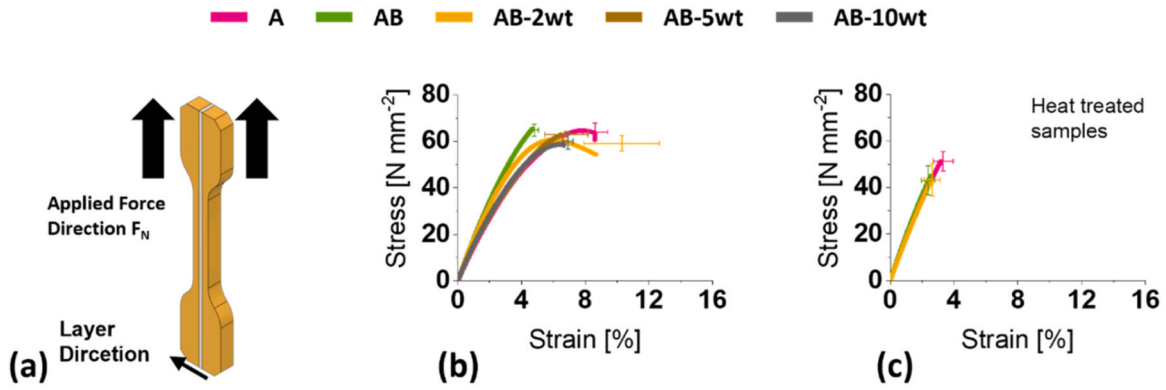

Fig. 8. Printing and applied force orientation of the YZX specimens (a), results of the tensile tests at room temperature (b), and of the heat-treated samples (c).

the polymer's thiol and methacrylate groups. This creates an inherent weak point and is susceptible to failure when force is applied in the layer direction. Especially in this orientation the amount of TEMs has a clear influence on the tensile strength, with AB-10 wt significantly showing the lowest value. It can be assumed that the more TEMs there are at the interface, the lower the adhesion between the two material types. However, all groups of specimens containing 5 wt% and 10 wt% of the TEMs achieved their intended purpose of separating the samples upon heating.

Fig. 9 and Fig. 10 display the fracture surfaces of the ZXY specimens, illustrating the failure of the specimen due to low adhesion between Specimen Type A and the DfD material.

This lack of adhesion is again attributed to the interaction between the thiol and methacrylate groups without any bonding occurring between the allyl and methacrylate groups.

4.4. Dynamic mechanical analysis (DMA)

4.4.1. YXZ orientation

The DMA showed that the DfD material had a significant effect on Type A at higher temperatures when placed in the YXZ orientation (Fig. 11**d**). At room temperature, all groups demonstrated similar storage moduli, yet all AB samples underwent a rapid decline at about ~ 50 °C (Fig. 11**a**). This decrease was not observable in Type A. The influence was confirmed by the first peak in the tanδ diagram at 50 °C. (Fig. 11**b**).

At this temperature, the DfD material has already reached its glass transition temperature and is altering the characteristics of the entire blend. Because of the narrow course of the G''-curve, T_g could alternatively be gained out of the maximum of the loss modulus, which was comparable to the tanδ maximum value (Fig. 11**c**). The narrow and high G''-curve suggested a highly regulated network in the DfD material,

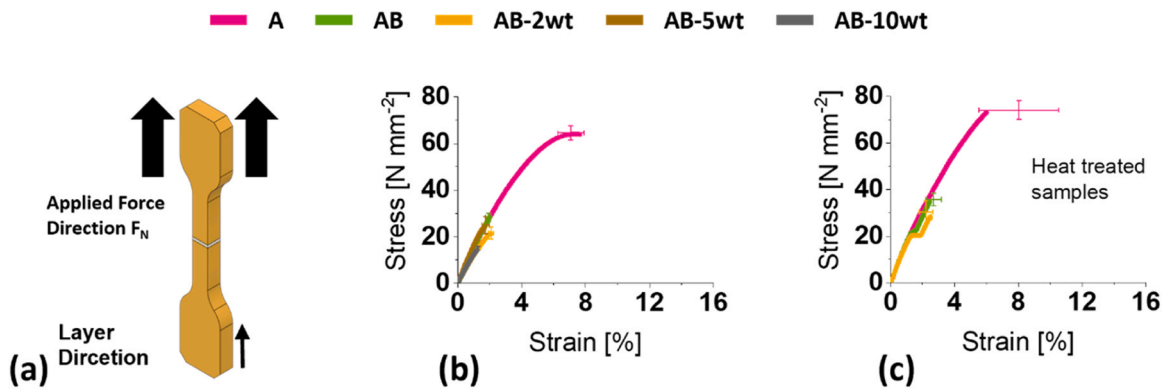

Fig. 9. Printing and applied force orientation of the ZXY specimens (a), results of the tensile tests at room temperature (b), and of the heat-treated samples (c).

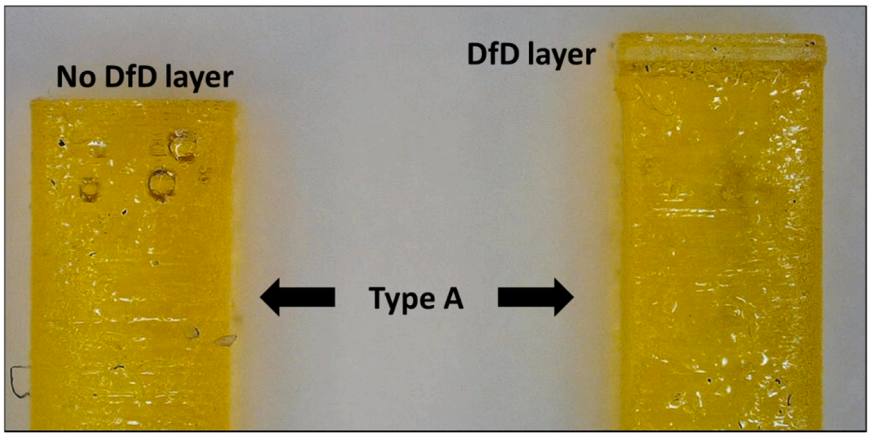

Fig. 10. Digital microscope images of the fracture surfaces of a specimen sample. The left part does not contain the DfD material, which only adheres to the right part. The failure of the specimen is due to adhesive rather than cohesive failure.

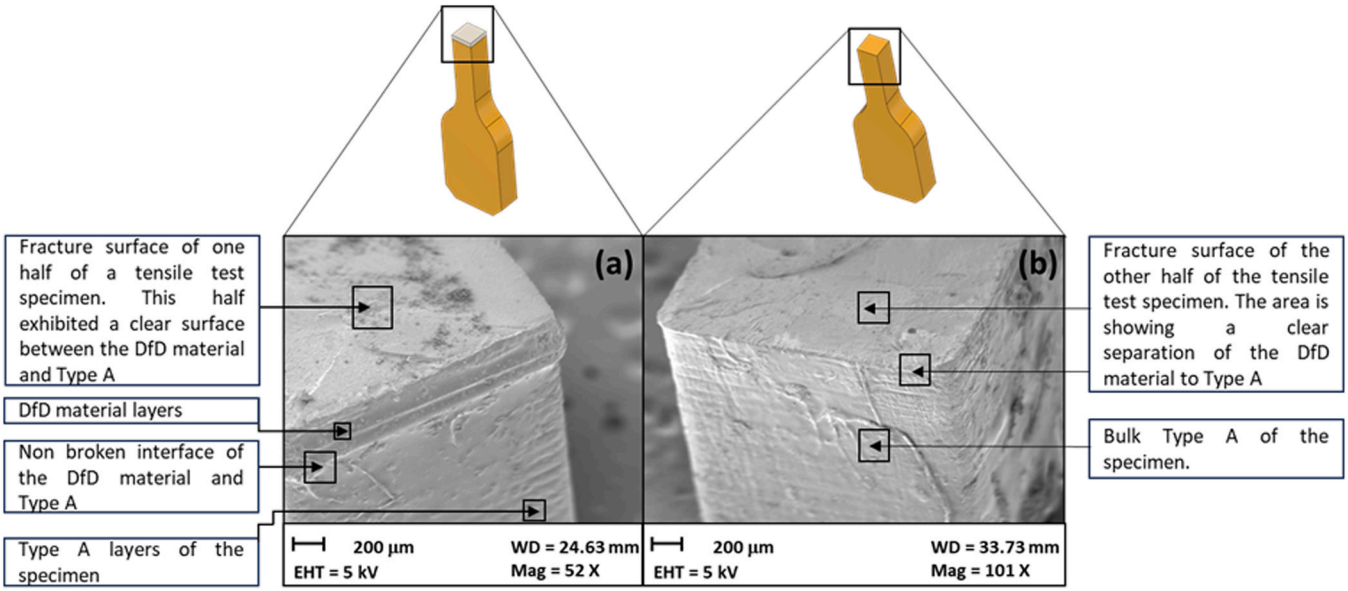

Fig. 11. Fracture surfaces of both parts of a tensile test specimen in ZXY direction. The DfD material sticks to one part of the specimen (a), while the separation happens between the DfD material and Type A. At the other part (b) no DfD material is visible.

coupled with a high energy dissipation ability. The well-regulated network and high energy dissipation of the DfD material are crucial for the disassembly ability of the device. Compared to a strongly cross-linked photopolymer, the network-regulation promotes a thermoplast-like behaviour of the DfD layer, which facilitates a more uniform deformation of the layer during expansion of the TEMs.

4.4.2. *YZX orientation*

The YZX orientation specimens contained the rectangular DfD layers across the whole component, along its long edge (Fig. 12**d**). The effect of the DfD material and TEMs on Specimen Type A's storage modulus was negligible in the YZX samples. Fig. 12**a, b, and c** demonstrate similar trends for all curves across the temperature range.

The results of the study highlighted that the properties are significantly affected by both the printing direction and the orientation of the DfD layer. Herein the quantity of the DfD material has a higher impact on the YXZ samples as a result of the applied force in DMA being perpendicular to the specimen, compared to the YZX samples. This was also visible in the tanδ and loss modulus diagram, where no second peak or regulation of the network was visible. However, all specimens containing 5 and 10 wt% TEMs were able to achieve complete separation upon heating.

4.4.3. *ZXY orientation*

The ZXY orientation DMA samples had the DfD material in the centre of the specimen when printed upright (Fig. 13**d**). The results of the ZXY samples showed a resemblance to the YXZ orientation, albeit to a greater extent. The storage moduli of all blends exhibited a pronounced reduction once surpassing 50 °C (Fig. 13**a, b, and c**).

Especially the first tanδ peak and the maximum value of G'' exhibited the highest peaks among all orientation groups. It should be noted that the samples were positioned in a consistent manner to ensure that the DMA clamp was in contact with the DfD material (Fig. 13**d**). Since there was no Type A material present around the DfD material and supporting it, as it was for other orientations, it was not surprising that the impact was more prominent.

4.5. *Dynstat impact strength*

The Dynstat test was used to evaluate the impact strength of the specimens. The different printing orientations and placements of the DfD layers can be seen in Fig. 14. The impact strength a_n [kJ m^{-2}] can be

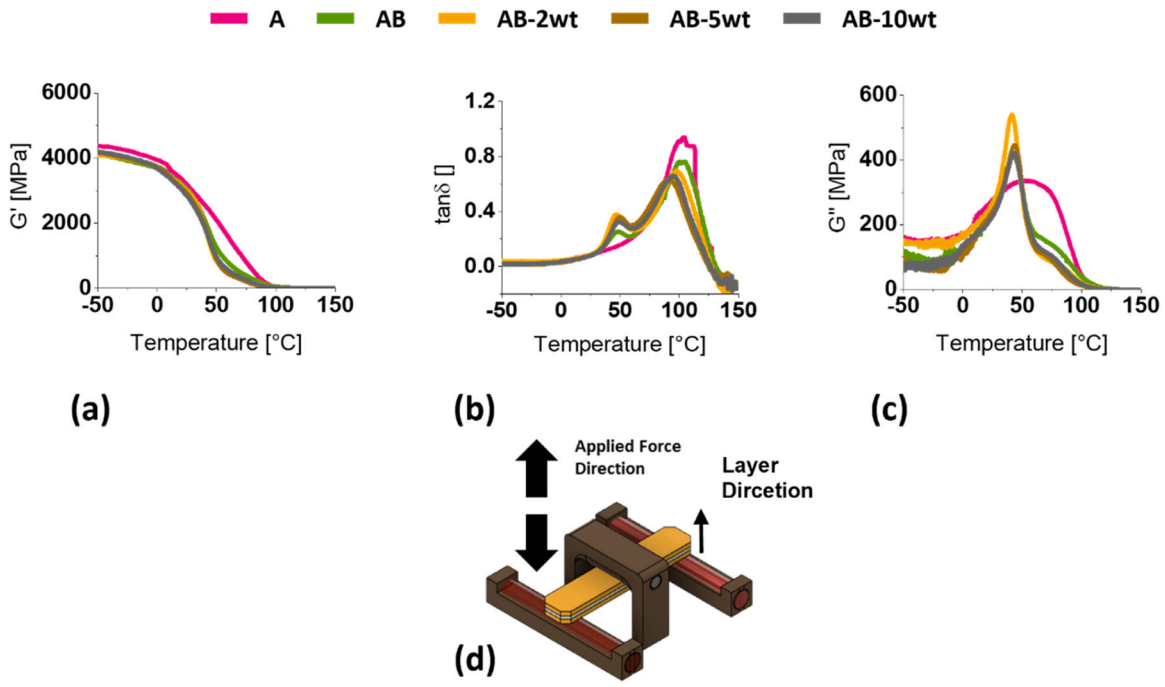

Fig. 12. Results of the (thermo)mechanical characterisation of the DfD material with TEMs in the YXZ orientation. (a) storage modulus (G'), (b) damping factor (tanδ), and (c) loss modulus (G''). (d) shows the arrangement and direction of the acting force on the specimen.

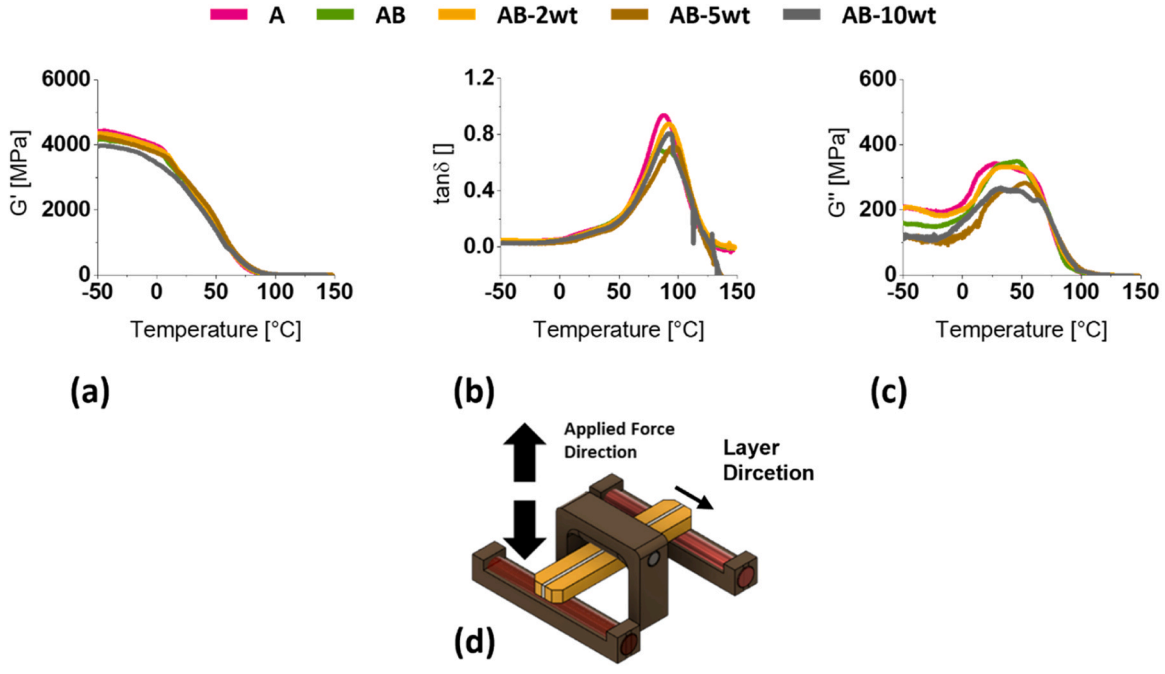

Fig. 13. Results of the (thermo)mechanical characterisation of the DfD material with TEMs in the YZX orientation. (a), storage modulus (G'), (b) damping factor (tanδ), and (c) loss modulus (G''). (d) shows the arrangement and direction of the acting force on the specimen.

calculated with the following equation:

$$a_n = \frac{w_n}{h * b} \quad (1)$$

where w_n is the impact energy absorbed by the specimen [kJ], h the height of the specimen [m] and b the width of the specimen [m].

The YXZ-specimens revealed the highest values, especially for Type A. Nevertheless, the impact strength was significantly reduced by approximately 50 % due to the incorporation the DfD material and the TEMs (Fig. 14**a**). It is assumed that the interface of the two materials can act as a weak spot of the sample, which led to an easier crack growth. Whilst the DfD system showed a greater impact on strength in YXZ samples, overall strengths were lower for all other orientations (YZX and ZXY). However, their blends exhibited a comparatively miner reduction in contrast to the Type A. The results showed that the DfD materials and TEMs do not affect the general impact strength of the YZX and ZXY orientation groups (Fig. 14**b, c**). The impact strength of the heat-treated samples decreased, particularly for YXZ. The significant decrease in

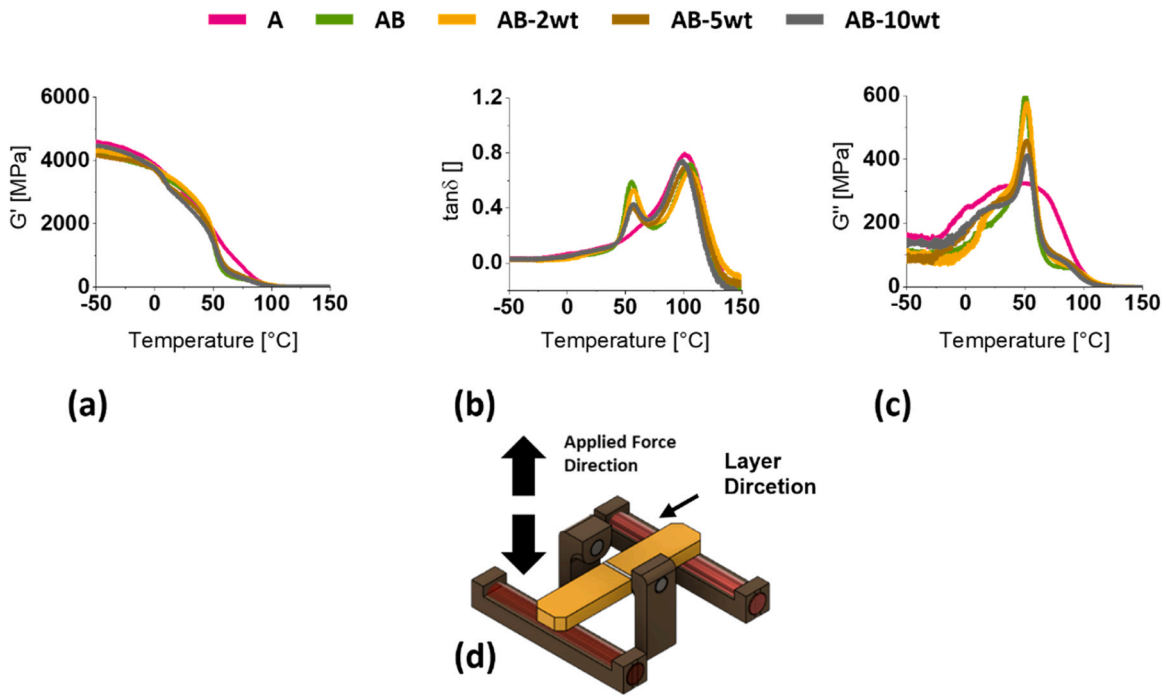

Fig. 14. Results of the (thermo)mechanical characterisation of the DfD material with TEMs in the ZXY orientation. (a), storage modulus (G'), (b) damping factor (tanδ), and (c) loss modulus (G''). (d) shows the arrangement and direction of the acting force on the specimen.

strength of Type A was particularly noteworthy since it was comparable to that of the AB and AB-2 wt samples after heating. Like the tensile test samples, the AB-5 wt and AB-10 wt specimens were unmeasurable due to full separation while undergoing the heating process.

It should be noted that none of the ZXY specimens fractured at the interface of the DfD material and Type A or inside the DfD Material in the Dynstat trial. The specimen fractured solely due to the substrate failure of Type A. Even though the ZXY specimens exhibited the least tensile strength, the junction between the two materials did not function as weak spot. All samples have fractured above the layer (Fig. 15), indicating sufficient bonding between the two materials. It can be demonstrated that, as long as the applied force is not perpendicular to the layer direction (as it is the case in the tensile test and the ZXY orientation), the multi-material components can still withstand a certain

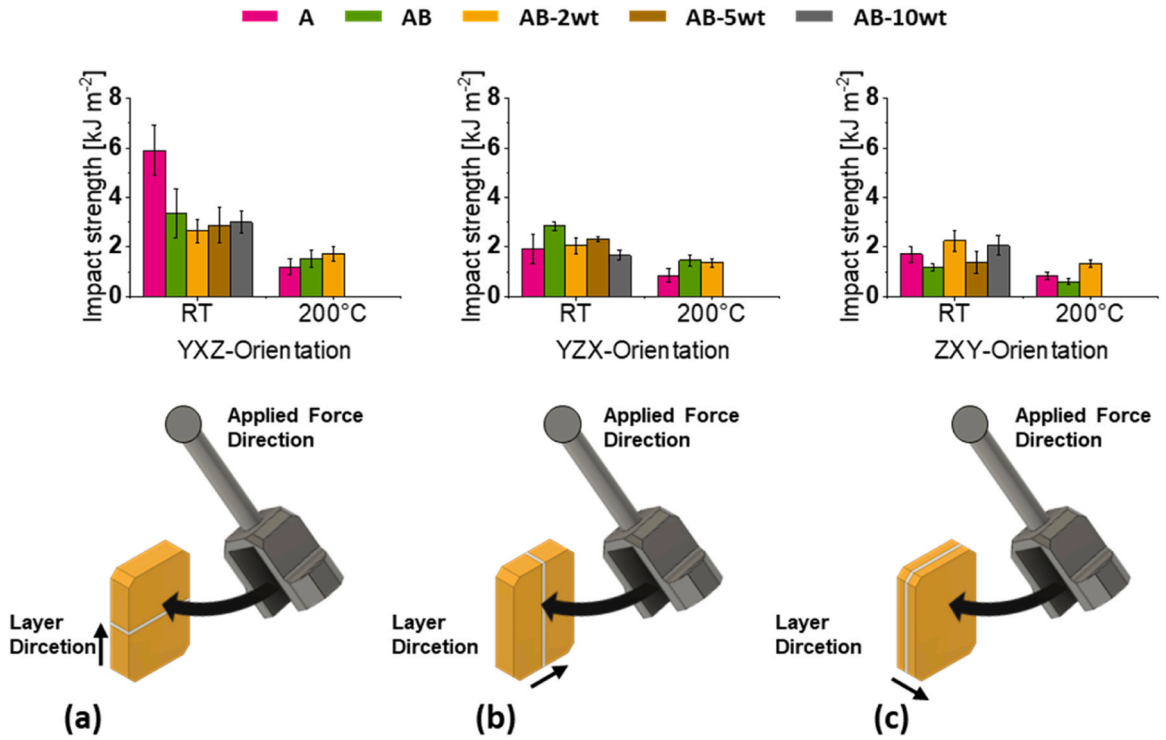

Fig. 15. Dynstat impact strength, measured with all printing orientations. (a) YXZ orientation, (b) YZX orientation, and (c) ZXY orientation. The left side of the diagrams (RT) represents the results measured at room temperature. The right side the results, which underwent the heat treatment.

load.

4.6. Disassembly experiments

The disassembly experiments investigated the potential for Design for Disassembly (DfD) of the introduced system through heat treatment of the specimens and a commercially available Molex cable connector. For this purpose, the specimen samples were heated in an oven for 10 min at 200 °C. The cable connector was heated in a special oven with a visible window, as explained in chapter 3.10. At this temperature, it was expected that the Thermally Expandable Microspheres (TEMs) would fully expand and reveal their disassembling potential. The key factor for successful disassembling is to embed the TEMs within a material having a lower glass transition temperature (T_g) than the TEM activation temperature. Furthermore, a regulated network with a high level of energy dissipation at the disassembly temperature would be beneficial. In this case, "regulated network" refers to the pronounced homogeneity of the allyl-thiol network formed by pure step-growth-, as opposed to homopolymerization, which normally leads to highly cross-linked photopolymers. This ensures that the (thermo)mechanical properties of the material change uniformly over a narrow temperature range and that the entire DfD material undergoes its transition from a glassy to a rubbery state simultaneously. It allows the TEMs to fully expand within the material. A more regulated network therefore leads to a sharp glass transition of the material and a more efficient adaption of the TEMs to the DfD material. As mentioned in chapter 3.2, 3.2, and 3.4 all samples containing 5 and 10 wt% TEMs separated completely during heating. All samples with 2 wt% did not separate and showed only minor changes in mechanical properties compared the Type AB samples. The majority of samples showed a clean surface on one side (absentness of DfD material and TEMs), while the other side contained both components (Fig. 16). The possibility of which side contains more DfD material is probably related to the distribution of the TEMs within the material. As the separation is mainly between Type A and the DfD material, the TEM density at the surface boundary is of particular importance.

Especially the cable connector could show the concept of Design for Disassembly to facilitate the recycling of electronic components (Fig. 17).

After being exposed to a temperature of 200 °C for a few seconds, the connector began to disassemble, allowing for easy removal of the inner parts (Fig. 17**f**). This result was made possible by the design, which contained the DfD material in the middle of the component as shown in Fig. 17**d**. The demonstration video, describing and showing the whole DfD process can be downloaded as supplementary content (Fig. 18).

Analysis of scanning electron micrographs of the tensile test specimens supported the assumption that the separation was mainly due to failure at the interface between material A and the DfD material (see Fig. 10). This assumption was expected on basis of the utilized material system: Specimen Type A comprised methacrylate groups, whilst the DfD material only consisted of allyl and thiol components. Only the thiol groups could bind to the methacrylate groups in Type A. Yet, the allyl-thiol system is essential because it creates a highly regulated network, due to its step growth polymerization manner. However, TEMs caused the failure of the DfD material during the disassembly process, leading to a successful separation of the components. Overall, the combination of both, the adhesive failure between the two materials and the ability of the TEMs to break down the DfD material led to the shown result.

5. Conclusion

This paper has demonstrated the Design for Disassembly (DfD) concept using additive manufacturing as the production method. The study utilised a combination of a hard matrix material (Type A) and a DfD material filled with Thermally Expandable Microspheres (TEMs) through a multi-material approach to produce components that can be easily dismantled.

The materials employed were adjusted to ensure compatibility and easy disassembly, while maintaining the same (thermo)mechanical properties, as the DfD layer would not be present in the component. It is imperative that the influence of the DfD layer is not noticeable at the operating temperature of a component, such as a cable connector at room temperature, to ensure that its effect is only visible when activated.

Especially the DfD material needed to fulfil certain requirements to be used as one, in terms of processability and material properties. To investigate the impact of the introduced system, rheology, and several (thermo)mechanical tests were performed, including tensile tests, DMA, and Dynstat impact strength tests. The properties of the entire component were affected by the additional DfD system, to varying degrees, which heavily relied on the layer orientation. Especially ZXY orientation exhibited the greatest impact of the additional DfD layers. Yet the amount of added TEMs only played a minor role. The primary factor affecting the results was the DfD material itself. At room temperature, the addition of 2 wt%, 5 wt%, or 10 wt% did not have a significant impact. If the force applied was not entirely orthogonal to the layer direction, only little effects could be observed. Here SEM measurements showed, that the failure of the specimens at RT was mainly due to adhesive failure between the two materials. However, due to the potential for moisture absorption of the DfD material over time, cohesive failure of the material may also occur, which was not further investigated. Due to the low layer thickness, which correlates to a small surface area exposed to moisture attack, the potential effect of moisture absorption was not considered but will be part of further investigations. When heated, the TEMs also led to the destruction of the DfD material, resulting in disassembly of the component due to cohesive and adhesive failure. The disassembly process was successfully demonstrated using a self-printed Molex cable connector, which separated after 10 minutes at 200 °C without requiring additional mechanical force. The concept of DfD shows therefore a promising method for commercial electronic components in the future, yet still needs to be developed further to be applicable in the proposed way.

CRediT authorship contribution statement

Jakob Ecker: Conceptualization, Methodology, Investigation, Writing – Original Draft, Writing – Review & Editing. **Robert Liska:**

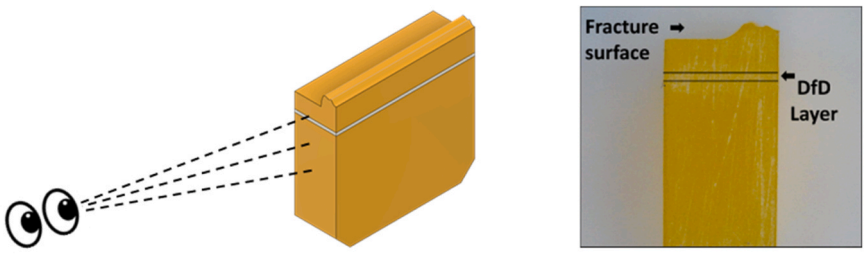

Fig. 16. Fractured ZXY sample from a Dynstat test viewed from the side. The specimen shows that it did not fracture at the location of the DfD material, but rather above the interface between the two materials.

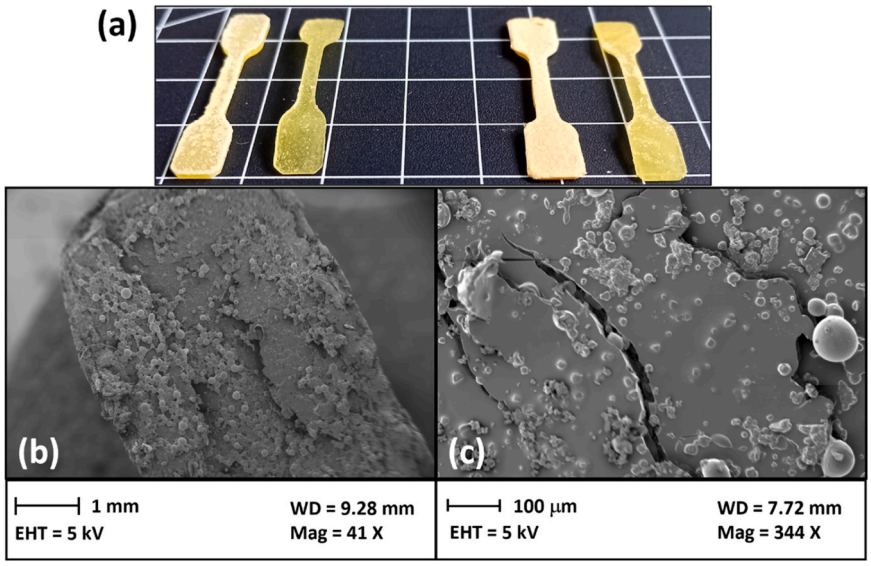

Fig. 17. (a) Tensile specimen with 5 wt% on the left and 10 wt% TEMs on the right, were observed to separate completely after 10 min at 200 °C. One surface was mostly clean while the other contained most residues of the DfD system. (b) SEM picture of a disassembled Dynstat sample. (c) Dynstat sample at higher magnification where the cracks from the TEMs are visible.

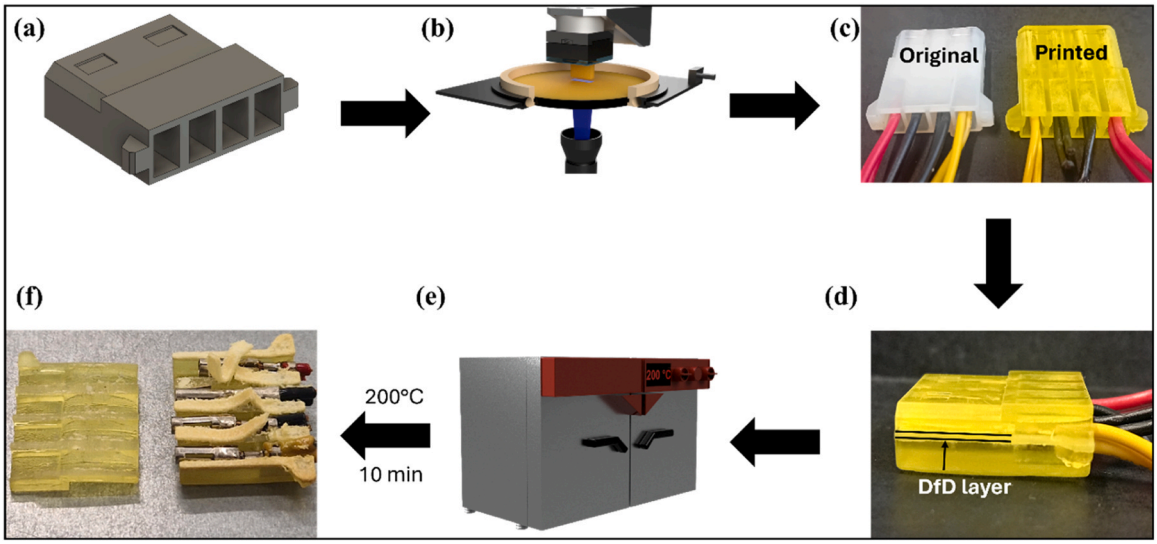

Fig. 18. Scheme of the DfD process. A component can be created via CAD, processed by 3D printing, and then disassembled through an external impulse. No additional mechanical force was needed to separate the part. (a) CAD designed part; (b) manufacturing process; (c) original object (left) and printed object (right); (d) integrated disassembly layer; (e) heat treatment for 10 min at 200 °C(f) dismantled part.

Conceptualization, Methodology, Resources, Writing – Review & Editing. **Jürgen Stampfl:** Conceptualization, Methodology, Resources, Writing – Review & Editing, Supervision, Funding acquisition.

Declaration of Competing Interest

The authors declare that they have no known competing financial interests or personal relationships that could have appeared to influence the work reported in this paper.

Data availability

Data will be made available on request.

Acknowledgements

The authors would like to thank Nouryon Netherlands for providing the Thermally Expandable Microspheres and Bruno Bock for the free sample of the trifunctional thiol. Special thanks to Jessica Sohl and Sarah Nistler for helping with the disassembly demonstration video. The authors acknowledge TU Wien Bibliothek for financial support through its Open Access Funding Programme.

Appendix A. Supporting information

Supplementary data associated with this article can be found in the online version at doi:10.1016/j.addma.2024.104394.

References

[1] B.C.P. Forti V, Kuehr R., Bel G., The Global E-waste Monitor 2020: Quantities, flows and the circular economy potential., in: U.N.U. (UNU)/United, Nations Institute for Training and Research (UNITAR) – co-hosted SCYCLE Programme, I.T. U.I.I.S.W. Association, B.G.R. (ISWA) (Eds.) 2020.

[2] Why is Recycling E-Waste so Difficult, 2023. https://techreset.com/itad-guides/why-is-recycling-e-waste-so-difficult/.

[3] S.M. Abdelbasir, S.S.M. Hassan, A.H. Kamel, R.S. El-Nasr, Status of electronic waste recycling techniques: a review, Environ. Sci. Pollut. Res. Int. 25 (17) (2018) 16533–16547, https://doi.org/10.1007/s11356-018-2136-6.

[4] M. Shahabuddin, M.N. Uddin, J.I. Chowdhury, S.F. Ahmed, M.N. Uddin, M. Mofijur, M.A. Uddin, A review of the recent development, challenges, and opportunities of electronic waste (e-waste), Int. J. Environ. Sci. Technol. 20 (4) (2022) 4513–4520, https://doi.org/10.1007/s13762-022-04274-w.

[5] S.C. Ligon, R. Liska, J. Stampfl, M. Gurr, R. Mulhaupt, Polymers for 3D printing and customized additive manufacturing, Chem. Rev. 117 (15) (2017) 10212–10290, https://doi.org/10.1021/acs.chemrev.7b00074.

[6] B. Wang, Z. Zhang, Z. Pei, J. Qiu, S. Wang, Current progress on the 3D printing of thermosets, Adv. Compos. Hybrid. Mater. 3 (4) (2020) 462–472, https://doi.org/10.1007/s42114-020-00183-z.

[7] U. Shaukat, E. Rossegger, S. Schlogl, A review of multi-material 3D printing of functional materials via vat photopolymerization, Polymers (Basel) 14 (12) (2022), https://doi.org/10.3390/polym14122449.

[8] 3D-Printing: From Multi-Material to Functionally-Graded Ceramic, Ceramic Applications, 2020, pp. 32-35.

[9] J. Stögerer, S. Baumgartner, A. Hochwallner, J. Stampfl, Bio-inspired toughening of composites in 3D-printing, Materials (Basel) 13 (21) (2020), https://doi.org/10.3390/ma13214714.

[10] K.R. Mulcahy, A.F.R. Kilpatrick, G.D.J. Harper, A. Walton, A.P. Abbott, Debondable adhesives and their use in recycling, Green. Chem. 24 (1) (2022) 36–61, https://doi.org/10.1039/d1gc03306a.

[11] C. Gorsche, C. Schnoell, T. Koch, N. Moszner, R. Liska, Debonding on demand with highly cross-linked photopolymers: a combination of network regulation and thermally induced gas formation, Macromolecules 51 (3) (2018) 660–669, https://doi.org/10.1021/acs.macromol.7b02321.

[12] M.A. Ayer, Y.C. Simon, C. Weder, Azo-containing polymers with degradation on-demand feature, Macromolecules 49 (8) (2016) 2917–2927, https://doi.org/10.1021/acs.macromol.6b00418.

[13] A.C. Ferahian, D.K. Hohl, C. Weder, L. Montero de Espinosa, Bonding and debonding on demand with temperature and light responsive supramolecular polymers, Macromol. Mater. Eng. 304 (9) (2019), https://doi.org/10.1002/mame.201900161.

[14] A.J. Inglis, L. Nebhani, O. Altintas, F.G. Schmidt, C. Barner-Kowollik, Rapid bonding/debonding on demand: reversibly cross-linked functional polymers via diels−alder chemistry, Macromolecules 43 (13) (2010) 5515–5520, https://doi.org/10.1021/ma100945b.

[15] ⟨https://www.nouryon.com/products/expancel-microspheres/blowing-agents/⟩.

[16] R.V.I. Gadhave, C.R. Gadhave, Application of thermally expandable microspheres in adhesives: review, Open J. Polym. Chem. 12 (02) (2022) 80–92, https://doi.org/10.4236/ojpchem.2022.122005.

[17] M.D. Banea, L.F.M. da Silva, R.J.C. Carbas, S. de Barros, Debonding on command of multi-material adhesive joints, J. Adhes. 93 (10) (2016) 756–770, https://doi.org/10.1080/00218464.2016.1199963.

[18] G.M. Beter Bain, Method and apparatus for bonding and debonding adhesive interface surfaces, USA, 2011, p. 14..

[19] G. Boothroyd, L. Alting, Design for assembly and disassembly, CIRP Ann. 41 (2) (1992) 625–636, https://doi.org/10.1016/S0007-8506(07)63249-1.

[20] M.S. Tavakoli, J. Mariappan, J. Huang, Design for assembly versus design for disassembly: a comparison of guidelines, ASME 2003 International Mechanical Engineering Congress and Exposition (2003) 389–395, https://doi.org/10.1115/IMECE2003-43951.

[21] G. Sossou, F. Demoly, G. Montavon, S. Gomes, An additive manufacturing oriented design approach to mechanical assemblies, J. Comput. Des. Eng. 5 (1) (2018) 3–18, https://doi.org/10.1016/j.jcde.2017.11.005.

[22] S.-K.S. Fan, C. Fan, J.-H. Yang, K.F.-R. Liu, Disassembly and recycling cost analysis of waste notebook and the efficiency improvement by re-design process, J. Clean. Prod. 39 (2013) 209–219, https://doi.org/10.1016/j.jclepro.2012.08.014.

[23] W.D. Li, K. Xia, L. Gao, K.M. Chao, Selective disassembly planning for waste electrical and electronic equipment with case studies on liquid crystaldisplays, Robot. Comput. -Integr. Manuf. 29 (4) (2013) 248–260, https://doi.org/10.1016/j.rcim.2013.01.006.

[24] C. Favi, M. Marconi, M. Germani, M. Mandolini, A design for disassembly tool oriented to mechatronic product de-manufacturing and recycling, Adv. Eng. Inform. 39 (2019) 62–79, https://doi.org/10.1016/j.aei.2018.11.008.

[25] G. Palmieri, M. Marconi, D. Corinaldi, M. Germani, M. Callegari, Automated disassembly of electronic components: feasibility and technical implementation, ASME 2018 International Design Engineering Technical Conferences and Computers and Information in Engineering Conference (2018), https://doi.org/10.1115/DETC2018-85302.

[26] F. Laverne, F. Segonds, N. Anwer, M. Le Coq, Assembly based methods to support product innovation in design for additive manufacturing: an exploratory case study, J. Mech. Des. 137 (12) (2015), https://doi.org/10.1115/1.4031589.

[27] G. Sossou, F. Demoly, S. Gomes, G. Montavon, An assembly-oriented design framework for additive manufacturing, Designs 6 (1) (2022), https://doi.org/10.3390/designs6010020.

[28] K. Liu, Q. Tan, J. Yu, M. Wang, A global perspective on e-waste recycling, Circ. Econ. 2 (1) (2023), https://doi.org/10.1016/j.cec.2023.100028.

[29] A. Vishwakarma, K. Kanaujia, S. Hait, Global scenario of E-waste generation: trends and future predictions, Global E-Waste Management Strategies and Future Implications (2023) 13–30, https://doi.org/10.1016/B978-0-323-99919-9.00013-1.

[30] R. Rautela, S. Arya, S. Vishwakarma, J. Lee, K.H. Kim, S. Kumar, E-waste management and its effects on the environment and human health, Sci. Total Environ. 773 (2021) 145623, https://doi.org/10.1016/j.scitotenv.2021.145623.

[31] M. Lopez, C. Reche, E. Perez-Albaladejo, C. Porte, A. Balasch, E. Monfort, E. Eljarrat, M. Viana, E-waste dismantling as a source of personal exposure and environmental release of fine and ultrafine particles, Sci. Total Environ. 833 (2022) 154871, https://doi.org/10.1016/j.scitotenv.2022.154871.

[32] M.D. Banea, L.F.M. da Silva, R.J.C. Carbas, Debonding on command of adhesive joints for the automotive industry, Int. J. Adhes. Adhes. 59 (2015) 14–20, https://doi.org/10.1016/j.ijadhadh.2015.01.014.

[33] W.A.S. Grellmann, Sabine, Kunststoffprüfung.

[34] K.H. Frank, K. Csizmadia, R. Kury, M. Gorsche, Hot Lithography - High precision 3D printing of flame retardant photopolymers for the electronics industry, RadTech, Florida, Hyatt Regency Orlando, 2022, p. 8.